Computational Biophysics of the Skin

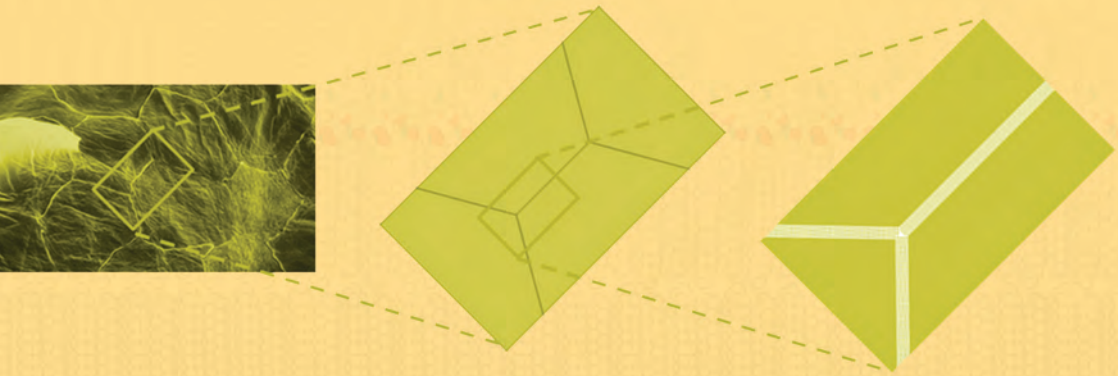

edited by
Bernard Querleux

Chapter 2

Dermal Component–Based Optical Modeling of Skin Translucency: Impact on Skin Color

Igor Meglinski,[a,b] Alexander Doronin,[b] Alexey N. Bashkatov,[a] Elina A. Genina,[a] and Valery V. Tuchin[a,c,d]

[a]*Research-Educational Institute of Optics and Biophotonics, Saratov State University, 83 Astrakhanskaya, Saratov, 410012 Russia*
[b]*The Jack Dodd Centre for Quantum Technology, Department of Physics, University of Otago, P.O. Box 56, Dunedin, 9054 New Zealand*
[c]*Laboratory of Laser Diagnostics of Technical and Living Systems, Institute of Precise Mechanics and Control of the Russian Academy of Sciences, 24 Rabochaya, Saratov, 410028 Russia*
[d]*Optoelectronics and Measurement Techniques Laboratory, University of Oulu, P.O. Box 4500, Oulu, FIN-90014 Finland*

tuchinvv@mail.ru

Computational modeling of skin color and/or skin reflectance spectra opens up new ways to investigate functional properties of human skin. Modeling of skin color and its variations associated with the physiological changes in human skin, such as blood oxy- and deoxygenation, melanin content, etc., is frequently required in various medical and biomedical applications. We present an open-access computational tool for online simulation of skin color and/or skin reflectance and transmittance spectra in real time. Human

Computational Biophysics of the Skin
Edited by Bernard Querleux

ISBN 978-981-4463-84-3 (Hardcover), 978-981-4463-85-0 (eBook)
www.panstanford.com

skin is presented as multi-layered medium. The variations in spatial distribution of blood, pheomelanin, eumelanin, index of blood oxygen saturation, hematocrit, and volume fraction of water are taken into account. The developed Monte Carlo (MC)-based calculator of spectra and color of human skin is supported by Compute Unified Device Architecture (CUDA), introduced by NVIDIA Corporation, that provides acceleration of modeling up to 10^3 times, allowing produce the results of simulation within seconds. The calculator is based on the object-oriented programming (OOP) paradigm and available online at www.biophotonics.ac.nz.

Examples of MC modeling of skin optical properties optimal for removal the tattoo or any other localized absorbing abnormality by laser thermolysis are also presented. This optimization is based on the laser wavelength selection and application of immersion optical clearing for enhancement of laser light selective absorption.

2.1 Introduction

In vivo measurements of human skin spectra serve as an important supplement to standard non-invasive optical techniques for diagnosing various skin diseases [1], such as venous ulcers, skin necrosis, and interstitial edema. However, the quantified analysis of the reflectance spectra is complicated by the fact that skin has a complex multilayered non-homogeneous structure with a spatially varying absorption coefficient, mainly determined by melanin pigmentation, oxygen saturation of cutaneous blood, index of erythema, contents of bilirubin, β-carotene, and other chromophores. Various approaches targeting the modeling of human skin reflectance spectrum and associated colors exist, but in our current work we apply the recently developed multipurpose graphics-processing unit (GPU)-accelerated MC tool for the needs of biophotonics and biomedical optics [2–4].

The description of optical radiation propagation within random media is based on the radiative transfer theory [5] that forms a basis of MC modeling of photons migration in biological tissues [6]. Originally introduced in biomedical optics for the counting of fluence rate distribution in biological tissues for the purpose of estimation laser radiation dose [7], in the last decades the MC approach has become a primary tool for a number of needs in biomedical optics. Incorporated with the computational model of

human skin [8] MC technique has been used for simulation of skin visual and near-infrared reflectance spectra [9,10], analysis of skin fluorescence excitation [11–13], simulation of optical coherence tomography (OCT) images of human skin [14,15], analysis of scattering orders, and OCT image formation [16–18]. The MC approach has been generalized for simulation of coherent effects of multiple scattering, such as enhancement of coherent back-scattering (CBS) and changes of temporal intensity correlation function depending on the dynamics of scattering particles [19,20]. Based on these developments a new approach of handling polarization has been introduced and some effects such as a helicity flip of circular polarization has been observed [21,22]. The obtained modeling results have been comprehensively validated by comparison with the known exact solution by Milne [23,24] and with the results of experimental studies of image transfer through the water solution of spherical microparticles of known size and density [25,26]. Meanwhile, a number of other MC algorithms has been developed in the past, see for example [27–30].

In this chapter, we discuss an MC approach specially designed for imitation of reflectance spectra and associated colors of human skin. The developed skin spectrum/color calculator utilizes seven-layered skin model corresponding to *Stratum corneum*, living epidermis, papillary dermis, upper blood net dermis, reticular dermis, deep blood net dermis, and subcutaneous fat. In the framework of the calculator, different modeling parameters can be independently varied, including concentration of blood, hematocrit, oxygen saturation, volume fraction of hemoglobin in erythrocytes, concentration of water, and thickness of the layers. Some examples of MC modeling of skin optical properties for practical use, such as tattoo and other absorbing abnormalities imaging and selective ablation by laser thermolysis, will be discussed in the framework of tissue optical clearing concept.

2.2 Skin Color Calculator

2.2.1 Online Object-Oriented Graphics-Processing Unit—Accelerated Monte Carlo Tool

Due to a number of practical applications in skin optics, the MC model undergoes continuous modifications and changes dedicated

to the inclusion of diverse properties of incident optical/laser radiation, configuration of the sources and detectors, structure of the medium and the conditions of light detection [8–30]. Past attempts to unify the MC codes [31] are mainly based on the use of structured programming. While structured programming is known for years, it limits the ability to handle a large code without decreasing its functionality and manageability [32]. In practice, the increasing diversity of the MC applications results to a substantial growth of the model's source code and leads to the development of a set of separate MC codes dedicated each for a particular purpose.

To generalize and unify the code for a multi-purpose use in various biomedical optics applications we apply the OOP concept. Object-oriented programming is widely used in mainstream application development and has been found extremely effective in design of complex multi-parametric systems, providing highly intuitive approach of programming [33]. The key features of OOP allow for the MC to be separated into logical components, described by objects.

Thus, the OOP approach significantly increases the efficiency of the model manageability and provides superior opportunities to generalize MC to combine previously developed MC models in a way to imitate a particular skin optics experiment taking into account various features of optical radiation and light-tissue interaction.

2.2.2 Graphics-Processing Unit Acceleration of MC

Launching of a large number ($\sim 10^8$–10^9) of photon packets and computing their interaction with medium and with the probe is a highly intensive computational process. Owing to a required computational performance, processing time has always been a significant issue in stochastic modeling, taking hours or even a few days to complete on a standard central processing unit (CPU). To achieve the supreme performance of simulation, a number programming approaches and optimizations of algorithms have been used in the past, including parallel and cluster computing [34,35].

We use recently introduced by NVIDIA Corporation parallel computing framework, known as Compute Unified Device Architecture (CUDA) technology, which provides an unlimited access to computational resources of graphic card: processor cores, different types of memory (of various capacity and speed) making

GPU a massive co-processor in parallel computations [34,35]. The graphic chip is capable of executing executes up to 30,000 threads simultaneously, without context switch performance losses and has a very fast (up to 4 Gbit/s) on-chip GDDR5 memory. Graphics-processing unit's shared memory has been used to store the intermediate results; constant memory is applied for data input, whereas the global memory is used to store parameters of photon objects (e.g., path-length, state of polarization, outlet angles, etc.).

The OOP MC model has been developed using CUDA 4.0 C/C++ and supports multiple GPUs. The hardware is presented by a MPICH2 cluster of four Tesla M2090/GeForce GTX 480 graphic cards with NVIDIA CUDA computing capability 2.0 totally having up to 5 Tflops of computational power on board. This cutting-edge graphic technology also incorporates a powerful set of instruments applied for optimized simulation of objects motion, rotation, reflection, ray-tracing, etc. The NVIDIA CUDA provides GPU-accelerated mathematical libraries, such as CULA, CUBLAS—Linear Algebra, CUFFT—Fast Fourier Transform, and CURAND—Random Number Generators [36]. Their incorporation into MC allows for speeding up the simulation of each photon packet up to 10^3 times.

2.2.3 Online Solution

With the rapid growth of the Internet, rich, browser-based applications have become more and more popular. Solutions such as Google Apps, Google Docs, online video sharing, and gaming portals have become a large part of our everyday life. In comparison with traditional desktop applications, they are much easier to deploy and update, as a capable Web-browser is the only requirement [37]. Leveraging modern, Web-based technology, we have created a free online MC computational tool for researchers in the area of biophotonics and biomedical optics [2,3]. On the server side, the tool is accelerated by CUDA GPUs. On the client side, a lightweight, user-friendly Web interface allows multiple clients to set up optical system parameters, perform modeling, and download results in a typical journal paper format. We have combined powerful GPU technology with a modern Web application development approach, allowing researchers to use, check, and validate our MC model using our group's GPU computing facilities [38].

A conceptual design of the online solution is schematically presented in Fig. 2.1.

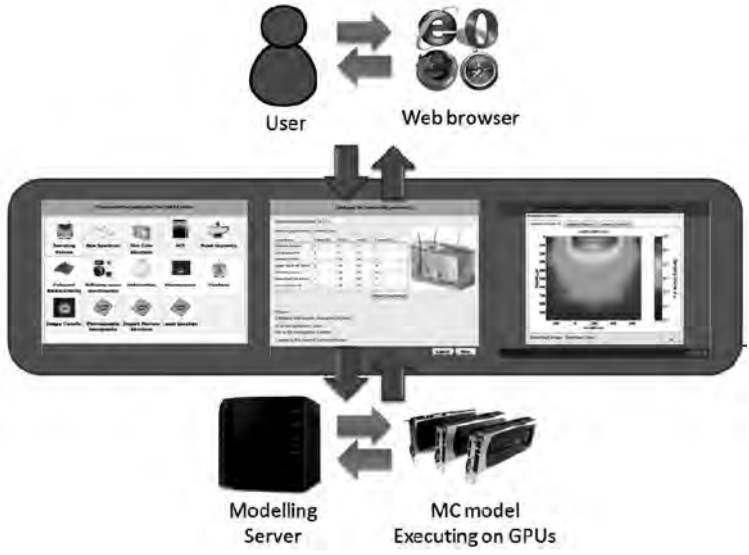

Figure 2.1 Schematic presentation of the online MC tool. The server hosts a Web frontend, which accepts the user's simulation requests and displays the obtained results. The developed components provide interoperability between the interactive user interface and GPUs, executing all heavy-duty MC-related tasks.

Integrating CUDA acceleration with the modern Web technologies, such as Microsoft Silverlight and ASP.NET Framework, the Online Object Oriented MC (O3MC) computational tool was developed [39]. The key idea behind O3MC development is the creation a universal computational tool to simulate the results of real experiments typically used in major applications in biomedical optics and related areas that could provide researchers with practical results nearly in real time.

Object-oriented programming and GPU implementations enable speeds up the procedure of MC simulation up to 10^3 times [39]. However, due to the multi-user architecture of the online solution, concurrent simulations by multiple clients significantly degrade performance of O3MC. For example, if one user accessing the O3MC can get the results in 4.3 seconds on TESLA M2090 GPU, 100 users accessing O3MC at the same time can be stacked in a queue and wait for 10–15 min.

Therefore, in framework of further development of O3MC to deal with the multi-user access we apply a peer-to-peer (P2P)

network [39]. The proposed P2P network consists of a set of computers, called nodes or peers, which communicate and share their GPUs (Fig. 2.2). The peers in P2P network are equal among each other, acting as both clients and servers. P2P approach has gained a lot of popularity in the recent years, especially in terms of multimedia content delivery and communication (e.g., BitTorrent, Skype).

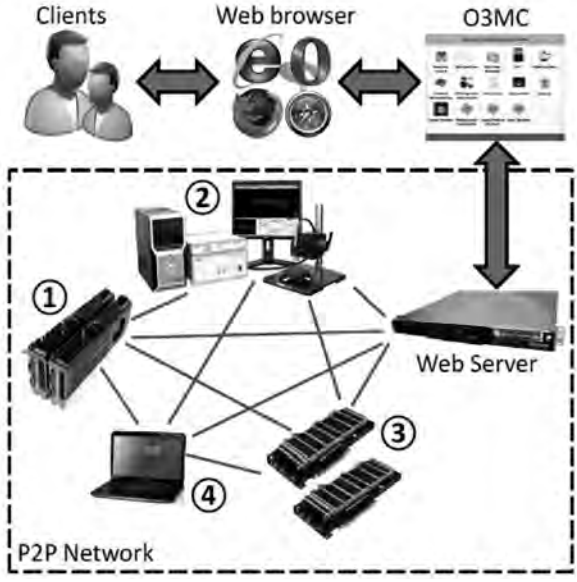

Figure 2.2 **Schematic presentation of P2P O3MC implementation.** Clients interact with the O3MC Web interface via a preferred Web browser. The server accepts O3MC simulation requests and keeps track of the participating peers. The P2P network consists of different computers equipped with the CUDA-supporting GPUs: (1) a workstation with two GeForce GTX 480 GPUs each 480 CUDA cores, 1540 Gigaflops of the peak single precision FPP/85 Gigaflops double precision FPP, 1536 GB of GDDR5 memory; (2) Thorlabs OCT imaging system workstation with Quadro FX580 featuring 32 CUDA cores, 512 MB GDDR3 memory; (3) computational server equipped with two Tesla M2090 GPUs each 512 CUDA cores, 1331 Gigaflops of the peak single precision floating point performance (FPP)/665 Gigaflops double precision FPP, 6 GB of GDDR5 memory; (4) Dell laptop with GeForce GT555M featuring 144 CUDA cores, 3072 GB GDDR3 memory. Adapted with permission from [39].

Web server hosts the online MC tool user interface, accepts O3MC simulation requests from clients, and keeps track of the other nodes (see Fig. 2.2). The nodes are responsible for sharing the information about currently queuing MC simulations, processing them on GPUs, uploading, downloading and hosting the outcomes (presented in a typical journal-paper format) among themselves without the need of the central server [39].

Figure 2.3 shows the welcome screen of the online O3MC tool available at http://www.biophotonics.ac.nz. This is a starting point providing access to a number of MC applications, including sampling volume, fluence rate distribution, skin spectra and skin color modeling, and other.

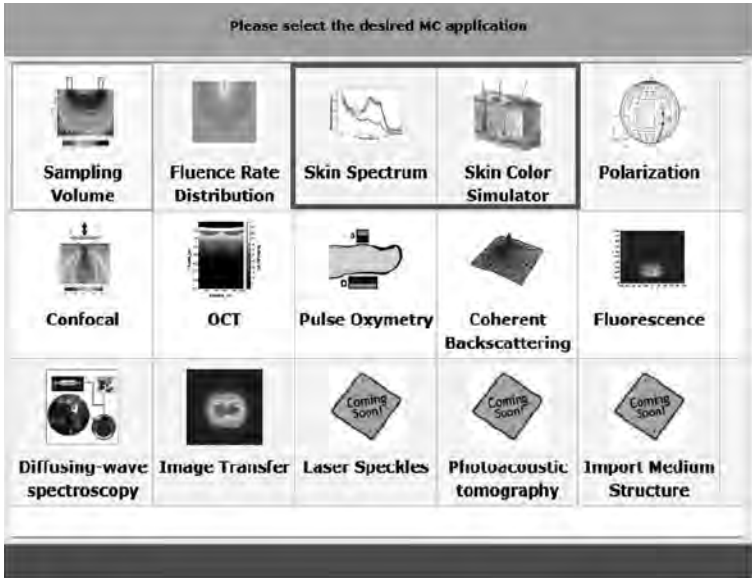

Figure 2.3 Front screen of the online O3MC tool. Each icon represents a different application. Skin color and skin spectra calculators are highlighted by frame. The application can be started by clicking the corresponding icon.

To use "skin spectrum" or "skin color simulator" applications a user should select the corresponding icon. Once the icon is clicked, the user will be taken to the page where he can either set up the detailed parameters of human skin model (Fig. 2.4) of the MC simulation or start the simulation using default parameters.

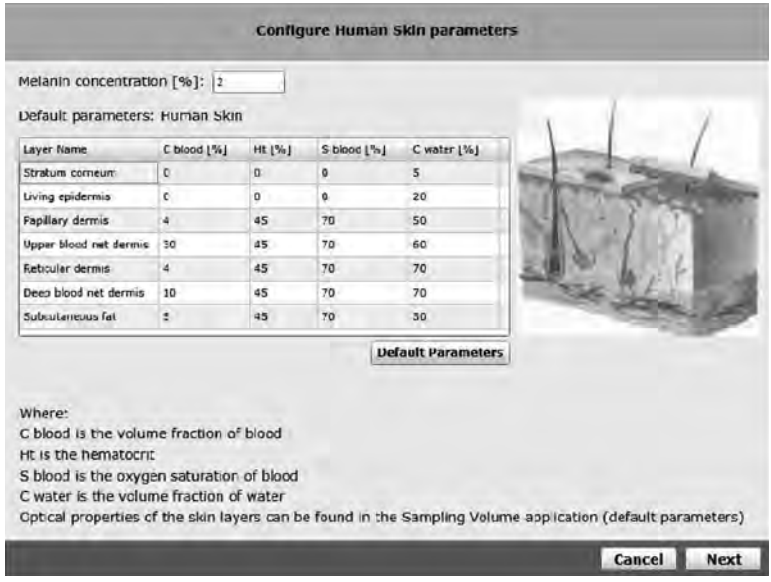

Figure 2.4 Configuring parameters of the seven layer human skin model, including blood concentration (C blood), hematocrit (Ht), the oxygen saturation of blood (S), fraction of water (C water).

When the parameters are configured, the server will perform a MC simulation and provide the user with the results in a typical journal paper format (see Section 2.3), which can be downloaded and further used.

2.3 Skin Spectra and Skin Color Simulation

2.3.1 Basics of MC

The MC is based on the consequent simulation of the photon packet trajectories as they travel through scattering medium [8,9]. The simulation of the photon trajectories consists of the following key stages: injection of a photon packet in medium, generation of photon path-lengths, generation of scattering events, definition of reflection/refraction at the medium boundary and detection. The random path length l a photon packet goes for a step i is given by

$$l = -\frac{\ln\xi}{\mu_s}, \tag{2.1}$$

where ξ is the computer-generated random number, uniformly distributed in the interval [0,1], μ_s is the scattering coefficient.

Internal reflections on medium boundary are taken into account by splitting the photon packet into reflected and transmitted parts. The weights of these parts are attenuated according to the Fresnel reflection coefficients [40]:

$$W = W_0 \left[1 - R_0(\alpha)\right] \cdot \prod_{p=1}^{M} R_p(\alpha) \tag{2.2}$$

Here, W_0 is the initial weight of the photon packet, M is the number of times the photon packet experiences a partial reflection on medium boundary, $R_p(\alpha)$ is the Fresnel reflection coefficient for the p-th photon-boundary interaction, $R_0(\alpha)$ is the Fresnel reflection coefficient for the initial photon-boundary interaction, where the photon packet enters the medium, α is the angle of incidence on the medium boundary [8]. The details of the reflection and refraction at the medium layers boundaries are given in detail in Refs. [8–12]. The simulation of the photon tracing within the medium is stopped when a photon packet has been scattered more than 10^4 times and does not depend on absorption. The counting of normalized skin spectra $I(\lambda)$ is based on the microscopic Beer–Lambert law and defined as follows [9,10]:

$$I(\lambda) = \frac{1}{N_{\text{ph}} W_0} \sum_{j=1}^{N_{\text{ph}}} W_j \exp\left\{ -\sum_{i=1}^{K_j} \mu_{\text{ai}}(\lambda) l_i \right\}, \tag{2.3}$$

where W_j is the final weight of the j-th photon packet defined by Eq. (2.3), K_j is the total number of scattering events for the j-th photon packet, λ is the wavelength, μ_{ai} and l_i are the medium-local absorption coefficient and the path length of photon packet at i-th step, respectively [8]. The total number of the photon packets N_{ph} typically used in spectra simulation is $\sim 10^8$–10^9.

2.3.2 Skin Model and Skin Tissues Optical Properties

To simulate the reflectance spectra of human skin, we adopted the seven layers skin model developed in Ref. [9,10]. The absorption of main skin chromophores [41] and skin layers are summarized in Fig. 2.5.

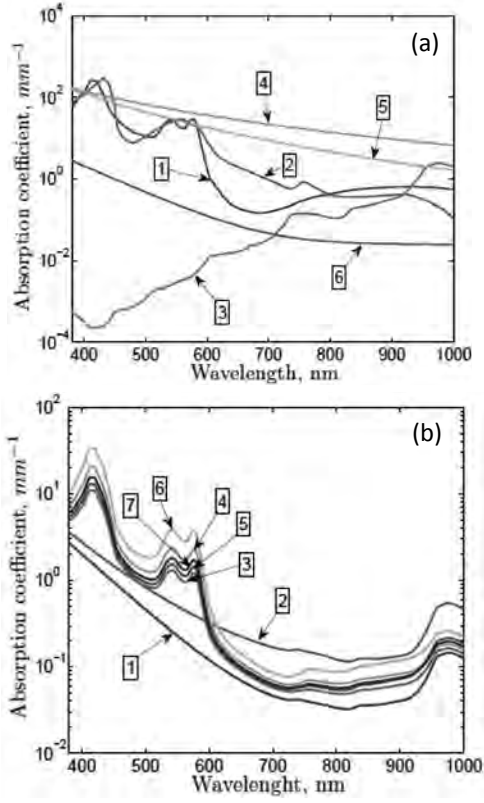

Figure 2.5 Absorption properties of skin tissues used in the simulation. (a) Absorption coefficients of major skin tissues chromophores: (1) oxy-hemoglobin, (2) deoxy-hemoglobin, (3) water, (4) eumelanin, (5) pheomelanin, and (6) baseline. (b) Absorption coefficients of the human skin layers counted by Eqs. 2.4–2.6. Adapted with permission from [44].

The absorption of skin layers takes into account concentration of blood (C_{blood}) in various vascular beds, oxygen saturation (S), water content (C_{H_2O}), melanin fraction (C_{mel}), and defined as [9,10]

$$\mu_a^{\text{Strat.corneum}}(\lambda) = (1 - C_{H_2O})\mu_a^{\text{baseline}}(\lambda) + C_{H_2O}\mu_a^{\text{water}}(\lambda) \tag{2.4}$$

$$\mu_a^{\text{Living epidermis}}(\lambda) = (1 - C_{H_2O})\{C_{\text{mel}}[B_{\text{mel}}\mu_a^{\text{mel}}(\lambda) + (1 - B_{\text{mel}})\mu_a^{\text{ph.mel}}(\lambda)] + (1 - C_{\text{mel}})\mu_a^{\text{baseline}}(\lambda)\} + C_{H_2O}\mu_a^{\text{water}}(\lambda) \tag{2.5}$$

$$\mu_a^{\text{Dermis}}(\lambda) = C_{\text{blood}}\{F_{\text{Hb}}F_{\text{RBC}}\text{Ht}[S\mu_a^{\text{oxy}}(\lambda) + (1-S)\mu_a^{\text{deoxy}}(\lambda)] + (1-\text{Ht})\mu_a^{\text{water}}(\lambda)\} + (1-C_{\text{blood}})(1-C_{H_2O})\mu_a^{\text{baseline}}(\lambda) + (1-C_{\text{blood}})C_{H_2O}\mu_a^{\text{water}}(\lambda) \quad (2.6)$$

Here $\mu_a^{\text{mel}}(\lambda)$ is the absorption coefficient of eumelanin, $\mu_a^{\text{ph.mel}}(\lambda)$ is the absorption coefficient of pheomelanin, B_{mel} is the volume fraction of the blend between two melanin types, $\mu_a^{\text{oxy}}(\lambda)$ is the absorption coefficient of oxy-hemoglobin, $\mu_a^{\text{deoxy}}(\lambda)$ is the absorption coefficient of deoxy-hemoglobin, $\mu_a^{\text{baseline}}(\lambda)$ is the absorption coefficient of other water-free tissue components, Ht is the hematocrit, F_{Hb} is the volume fraction of hemoglobin in a single erythrocyte, and F_{RBC} is the volume fraction of erythrocytes. The actual values of these parameters are presented in Table 2.1. C_{mel} varies within the ranges 0–45%.

Table 2.1 Parameters of skin layers, used in the simulation [9,10]

Layer	d (μm)*	Ht	F_{Hb}	F_{RBC}	C_{H_2O}	C_{blood}
Stratum corneum	20	0	0	0	0.05	0
Living epidermis	150	0	0	0	0.2	0
Papillary dermis	250	0.4	0.99	0.25	0.3	0.04
Upper blood net dermis	330	0.45	0.99	0.25	0.4	0.3
Reticular dermis	1830	0.45	0.99	0.25	0.5	0.04
Deep blood net dermis	1910	0.5	0.99	0.25	0.5	0.1
Subcutaneous fat	8000	0.45	0.99	0.25	0.6	0.05

*d is the thickness of the layer.

The scattering coefficients of skin layers (Fig. 2.6) are approximated basing on combination of Mie and Rayleigh scattering suggested in Ref. [42], as

$$\mu_s^{\text{Rayleigh}}(\lambda) = 2.2 \times 10^{11} \times \lambda^{-4}, \quad (2.7)$$

$$\mu_s^{\text{Mie}}(\lambda) = 11.74 \times \lambda^{-0.22}, \quad (2.8)$$

$$\mu_s^{\text{Layer}}(\lambda) = N[\mu_s^{\text{Rayleigh}}(\lambda) + \mu_s^{\text{Mie}}(\lambda)], \quad (2.9)$$

where N is the coefficient representing the fraction of scattering centers in the skin tissue, varying in a range 1 to 10.

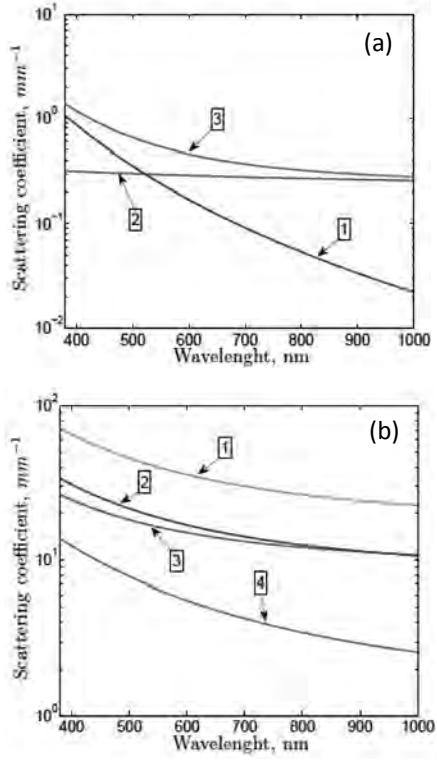

Figure 2.6 Scattering properties of tissues used in the simulation. (a) Reduced scattering coefficients: (1) Rayleigh scattering by Eq. 2.7, (2) Mie scattering by collagen fibers by Eq. 2.8, (3) the combined Rayleigh and Mie scattering by Eq. 2.9. (b) Scattering properties of human skin layers: (1) *stratum corneum*; (2) epidermis; (3) dermis; (4) subcutaneous fat. Adapted with permission from [44].

The skin reflection spectrum is modeled assuming that absorption and scattering coefficients of the layers of human skin are changed over the wavelength range (380–1000 nm) as presented in Fig. 2.6. This approach significantly enhances the modeling and allowed one to improve the overall quality of the outcomes.

Converting the spectral power distribution $I(\lambda)$ to the CIE XYZ coordinates and then to the actual RGB-gamut color images is done using the standard CIE 2° observer/tristimulus values utilizing D65 illuminant. The resulting images have been textured using a human skin surface BRDF mask [42].

2.4 Modeling Results

The online GPU-accelerated MC approach, presented above, has been used for both skin spectra and associated skin color simulations. Figure 2.7 presents the results of the modeling of human skin spectra and associated skin colors with various blood concentration and melanin content. The obtained results of skin spectra modeling are well agreed with the results of experimental measurements, e.g., by using the standard Ocean Optics spectrophotometer (Fig. 2.8).

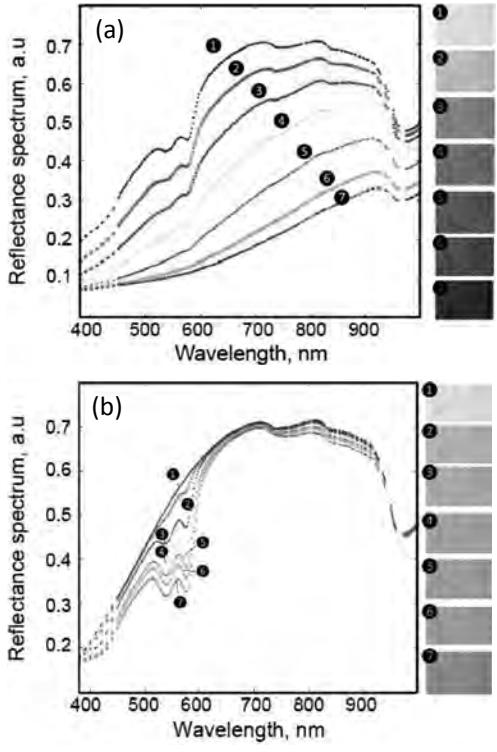

Figure 2.7 The results of MC simulation of human skin spectra (left) and corresponding colors (right) while varying the melanin content in living epidermis (a)—(1): 0%, (2): 2%, (3): 5%, (4): 10%, (5): 20%, (6): 35%, (7): 45%—and (b) while varying the blood concentration in the layers from papillary dermis to subcutaneous tissue: (1) 0%, (2) 2%, (3) 5%, (4) 10%, (5) 20%, (6) 35%, (7) 45%, respectively. The melanin concentration is 2% and fraction between eumelanin and pheomelanin is 1:3. Adapted with permission from [44].

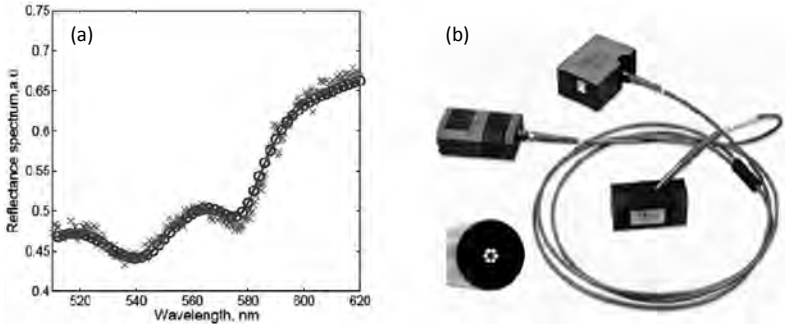

Figure 2.8 (a) Human skin reflectance spectrum simulated by the developed MC model (circles) compared with the results (crosses) obtained in vivo by a High-Resolution spectrometer (Ocean Optics USB4000). (b) Standard Ocean Optics USB4000 spectrometer and QR400-7-VIS-NIR probe (adapted from the manufacturer's Web site). Adapted with permission from [44].

Figure 2.9 displays the experimental results [43] for different parts of a human body in chromaticity coordinates plotted in the CIE 1931 color space in comparison with the results of MC simulation. It is clear that the experimental results and computational results are in a good agreement with each other.

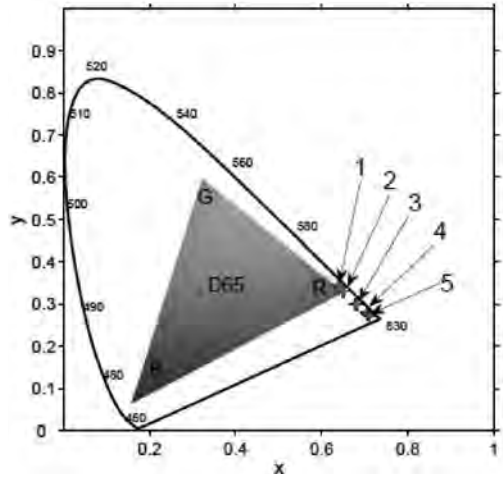

Figure 2.9 Chromaticity coordinates for fingernail (1), finger (2), palm (3), wrist (4) and forearm (5): crosses display experimental data and circles—the results of computer O3MC simulations. Adapted with permission from [44].

The design of the CIE 1931 color space splits the concept of color into brightness and chromaticity. The black contour in Fig. 2.9 is the spectral locus with the corresponding wavelengths. D65 is the standard daylight illuminant used in the O3MC model. The triangle represents a color gamut that can be reproduced by a standard computer monitor. As one can see the modeled tissue colors outside the gamut cannot be displayed properly on a standard color reproduction device and require a conversion procedure. Moreover, the diagram does not allow displaying of the actual brightness (luminance) of the colors. However, the actual colors are observed by a naked eye during the experiment.

To make the luminance visible, we converted the modeled CIE chromaticity coordinates into the Lab color space. Figure 2.10 shows experimentally observed and computer simulated near-IR transmission colors of different parts of a human arm, presented in CIE 1976 L*a*b* color space. The simulation is done for the actual experimental geometry and the fiber probe position used to collect the data. The simulated CIE 1976 L*,a*,b* coordinates in the color space, plotted in Fig. 2.10, are presented in Table 2.2 with the converted sRGB colors.

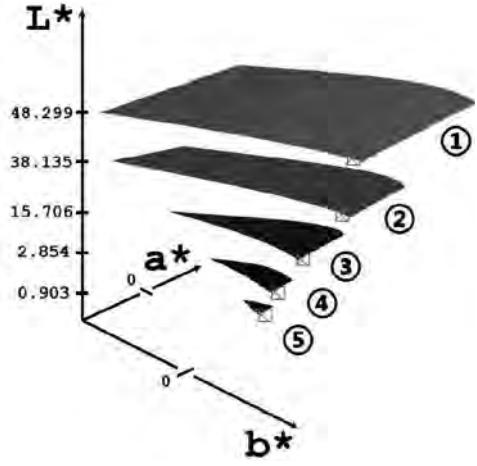

Figure 2.10 The changes of human skin color presented in CIE 1976 L*a*b* color space simulated by the developed MC model (crosses) compared with the results of measurements/observations in vivo (squares) for near-IR light transmitted through the various parts of human body: (1) fingernail, (2) finger, (3) palm, (4) wrist, (5) forearm. Adapted with permission from [44].

Table 2.2 The results of the MC simulation of skin color CIE coordinates in L*,a*,b* color space

Sample	L*	a*	b*	Standard deviation	sRGB Color
Fingernail	48.299	67.372	68.396	0.001	
Finger	38.135	62.883	54.705	0.001	
Palm	15.706	44.938	24.774	0.001	
Wrist	2.854	19.824	4.601	0.001	
Forearm	0.930	7.024	1.532	0.001	

Note: The standard deviation is calculated between the experimental data and the modeling output. CIE XYY coordinates converted to sRGB values are presented the resulting color in sRGB column.

Observing the effect of the changes of tissues color due to, for example, changes of blood and/or melanin content, and variations in blood oxygenation, is of a potential use for the practical diagnostic purpose and bioengineering applications. These changes can be quantified and characterized with the developed MC model.

2.5 Simulation of Skin Tattoo: Toward Its Effective Removal

2.5.1 Introductory Remarks

In this section, we present one of the examples of modeling of skin optical properties for some practical use: to optimize tattoo removal by laser thermolysis [47–50]. This optimization is based on the laser wavelength selection and application of immersion optical clearing [51–54] for enhancement of laser light absorption by tattoo pigments or any other localized absorbing substance (for example, malignant neoplasm) lying at some depth in the skin.

Nano-sized pigmented ink particles used for tattoo are located within dermis fibroblasts and mast cells, predominantly in a perivascular region. Red and NIR laser radiation penetrates deeply

into skin and it is absorbed more or less strongly by blue, green, and black tattoo pigments included in the composition of the most tattoos [47]. Although, short-wavelength radiation is well absorbed by tattoo pigments, the use of visible lasers is limited by a strong light scattering in skin and hemoglobin absorption.

The immersion optical clearing (IOC) based on the impregnation of tissue by an optical clearing agent (OCA) can improve laser tattoo removal due to reduction of light scattering of the upper tissue layers and correspondingly due to more effective laser beam delivery to the embedded ink particles [47–50]. The major mechanisms of IOC are well discussed in literature (see, for example, Refs. [51–54]) and can be explained in terms of refractive index matching concept because exogenous OCAs having a high index of refraction as penetrating into tissue and dissolving by interstitial fluid (ICF), match the refractive indices of scattering centers (collagen and elastin fibers) and ICF. Most of the OCAs are hyperosmotic liquids and thus intensively dehydrate tissue and therefore provide its temporal and reversible shrinkage, which also lead to better optical homogeneity of tissue and its lesser thickness. All these phenomena give the better penetration for light beams at their transportation in tissues, in particular in skin.

A number of laser diagnostic, surgery, and therapy technologies may have a significant benefit at a reversible skin optical clearing. However, slow diffusion of OCAs, such as glucose or glycerol water solutions, through human skin barrier makes practical application of IOC difficult. To overcome barrier function of skin epidermis a number of different chemical and physical methods such as skin stripping, microdermabrasion, laser fractional ablation of skin surface, iontophoresis, ultrasound, laser induced photomechanical waves, and needle-free injection were proposed [51–54].

In our work we use two different types of skin fractional ablation using lamp and laser (fractional laser microablation (FLMA)) techniques. The fractional ablation of SC can be done using a variety of light sources and delivery optics, including application of lenslet arrays, phase masks, and matrices of exogenous point-wise absorbers. The lamp technique is based on creation of the lattice of damaged micro-zones of stratum corneum (SC) by multi-dot intensive lamp heating of skin surface via transparent appliqué with many black dots, which absorb light and locally heat SC [55,56]. For the optimized procedure, a long-term effect of such damage is

only the transient deterioration of skin barrier function, because no any damage to viable tissue can be provided. That leads to the local increase of OCA's permeability via SC.

FLMA technique is one of the relatively safe and minimally invasive methods used to administer not only OCAs and drugs, but also micro and nanoparticles into the skin at sufficiently large depth in comparison with surface ablation and mechanical treatments because of the low area of skin damage and, therefore, reduced risk of infection [57].

Figure 2.11 illustrates how fractional ablation combined with IOC works for in vitro testing of human skin sample with the modeled black ink tattoo at fractional ablation of SC and glycerol application during 24 hours [49]. Tattoo is poorly recognized on the right image and clearly seen on the right image and dot areas of ablated skin via which glycerol penetrates are also well seen. Evidently, that this demonstration is valid for imaging of any in-depth absorbing pathology of the skin.

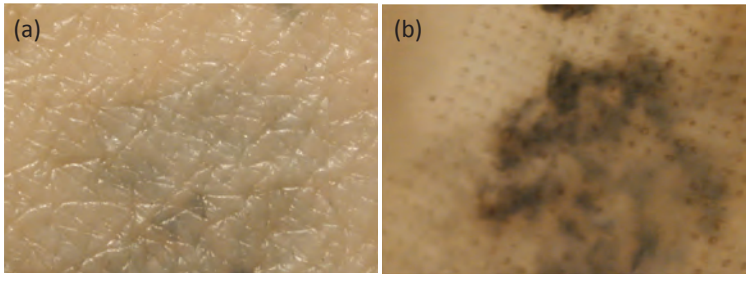

Figure 2.11 In vitro images of skin sample surface with black ink tattoo model: before processing (a) and after skin fractional ablation (lamp/transparent appliqué with many black dots) and glycerol application during 24 h (b) [49]. Tattoo is clearly seen on the right image (b) and dot areas of ablated skin are also well seen. Image (b) is done with polarization filtering.

Figure 2.12 illustrates the possibility of in vivo enhancement of tattoo imaging using skin surface preprocessing by the cyanoacrylate glue-stripping technique allowed for rapid and complete SC removal and glycerol delivery under pressure. There are shown unadjusted pre- (a) and post-glycerol (b) photographs of the treated skin region. Figures 2.12c,d are close-ups of the areas indicated in Figs. 2.12a,b, respectively. Enhanced visualization of the vasculature of the skin is also well seen.

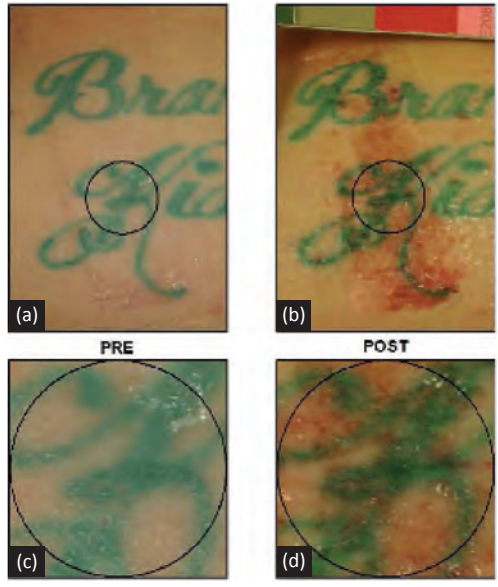

Figure 2.12 In vivo raw images pre (a and c) and post (b and d) glycerol application for a patient with the preprocessed skin by cyanoacrylate glue-stripping technique allowed for rapid and complete SC removal. A 100%-glycerol was used as an OCA, which was delivered into skin under pressure. The fluid pressure was maintained through continuous addition of glycerol from a dispenser using regulated compressed air over a separate glycerol in order to maintain a pressure of 30–70 mmHg for 30–60 min. After the bandage was drained through the fluid access port and removed, any remaining glycerol was wiped away with a paper towel. The intensification of the ink vision and the ability to visualize vasculature is seen in the post glycerol treatment (b and d) [48].

2.5.2 Skin Model and MC Simulation

The efficiency of laser radiation delivery to the skin sites where tattoo pigment is localized can be evaluated on the basis of MC simulations for variable optical properties of skin layers due to tissue clearing potency. We will consider that the absorption properties of skin are mainly determined by the absorption of melanin, water, and blood hemoglobin; as well as scattering is determined by the tissue structure components, such as collagen/elastin fibrils of dermis, mitochondria, and nuclei of epidermal cells.

In accordance with the optical and the structural-morphological properties of skin, the six-layer skin model was used [49,50] with the main parameters presented in Table 2.3 [58].

Table 2.3 Parameters of skin layers used in the MC simulations [58]

Skin layer	Thickness (μm)	Refractive index	Water content (%)	Blood content (%)	Scattering coefficient of a blood-less tissue at 577 nm cm^{-1}	Mean vessel diameter (μm)
Epidermis & SC	100	1.45	60	0	300	—
Basal membrane	15	1.40	60	0	300	—
Dermis & upper blood plexus	200	1.38	75	1.7	120	6
Reticular dermis	1500	1.35	75	1.4	120	15
Dermis & lower blood plexus	200	1.38	75	1.7	120	6
Subcutaneous adipose tissue	3000	1.44	5	0	130	—

In the visible and NIR spectral ranges the absorption coefficient of each skin layer is defined as

$$\mu_{ak} = B_k C_k \mu_a^{bl}(\lambda) + (1 - B_k - W_k)\mu_a^{bg} + M_k \mu_a^{mel}(\lambda) + W_k \mu_a^{w}(\lambda), \tag{2.10}$$

where k = 1, …, 6 is a layer number, B_k and W_k are the volume fractions of blood and water in the each layer; for the melanin containing layers (epidermis and basal membrane) M_k = 1, for the other skin layers M_k = 0; μ_a^{bl}, μ_a^{mel}, μ_a^{w}, and μ_a^{bg} are the absorption coefficients of blood, melanin, water and background matter (collagen) of tissue, respectively (in the framework of the model μ_a^{bg} is assumed to be wavelength independent and equal to 0.15 cm^{-1} [58]); C_k is a dimensionless correction factor. The correction factor

is a number from 0 to 1 and taking into account the fact that blood is localized in vessels rather than distributed homogeneously in the skin dermis. If the blood vessel diameter is large enough, and light does not penetrate to the inner part of the vessel, then hemoglobin of the interior part has not to be taken into account as an absorber; and in this case, the correction factor will be considerably smaller than unity. Otherwise, for thin vessels the correction factor is close to unity. Taking into account that the correction factor depends on the vessel diameter, we used in the model the following empirical expression [49,50]:

$$C_k = \frac{1}{1 + a(0.5\mu_{\mathrm{a}}^{\mathrm{bl}} d_k^{\mathrm{ves}})^b}, \tag{2.11}$$

where d_k^{ves} is the blood vessel diameter in centimeters and $\mu_{\mathrm{a}}^{\mathrm{bl}}$ should be expressed in inverse centimeters. If blood vessels lying in parallel to the skin surface are illuminated by a collimated light beam a = 1.007 and b = 1.228, while for the diffuse illumination of the vessels a = 1.482 and b = 1.151. The blood optical properties (i.e., anisotropy factor and both absorption and scattering coefficients) were calculated on the basis of algorithm described in detail in Ref. [59]. In the framework of the modeling, it was assumed that degree of hemoglobin oxygenation is 0.8 (oxygenation for arterial blood is 0.9 and that for venous blood is 0.7) and value of blood hematocrit is of 0.4.

The scattering coefficient of skin layers is defined as

$$\mu_{\mathrm{sk}}(\lambda) = B_k C_k \mu_{\mathrm{s}}^{\mathrm{bl}}(\lambda) + (1 - B_k)\mu_{\mathrm{sk}}^{\mathrm{bg}}(\lambda) \tag{2.12}$$

Here

$$\mu_{\mathrm{sk}}^{\mathrm{bg}}(\lambda) = \mu_{\mathrm{sk}}^{0}\left(\frac{577}{\lambda}\right)$$

is the scattering coefficient of bloodless tissue [58]; μ_{sk}^{0} is the scattering coefficient of bloodless tissue at the wavelength 577 nm (see Table 2.3); λ is expressed in nanometers.

The anisotropy scattering factor is expressed in the following form:

$$g_k(\lambda) = \frac{B_k C_k \mu_s^{bl}(\lambda) g^{bl} + (1 - B_k)\mu_{sk}^{bg}(\lambda) g^{bg}(\lambda)}{\mu_{sk}(\lambda)}, \tag{2.13}$$

where

$$g^{bg}(\lambda) = 0.7645 + 0.2355\left[1 - \exp\left(-\frac{\lambda - 500}{729.1}\right)\right]$$

is the scattering anisotropy factor of bloodless tissue [58]. The absorption coefficient of melanin is described by the following empirical expression [58]:

$$\mu_a^{mel}(\lambda) = A\exp\left(-\frac{\lambda - 800}{182}\right), \tag{2.14}$$

where A is the ratio of the optical density of pigmented skin layer (epidermis and basal membrane) to their thickness. In the model A was taken as 0.87 cm^{-1} for epidermis and 13.5 cm^{-1} for basal membrane [58].

2.5.3 Skin Immersion Optical Clearing and Tattoo Modeling

The optical clearing of different skin layers was simulated using Mie scattering theory [60], which requires the knowledge of the refractive indices of skin scatterers and surrounding interstitial fluid (ICF), and also sizes of the scatterers. Calculations for epidermis and basal membrane have been performed using the model of spherical particles, since cell mitochondria are the main scatterers for epithelial tissues, while for dermis the model of cylindrical particles was used, because of fibrous structure of dermis [61]. As the particle size distribution and the corresponding packing factor of the scatterers are unknown, monodisperse, so-called Mie-equivalent particles, were used for the simulation.

The scattering coefficient of the epithelial skin layers was calculated in the following form [60]:

$$\mu_s(\lambda) = \frac{3}{4}\frac{\varphi}{\pi a_{sph}^3}\pi a_{sph}^3 Q_s(a_{sph}, n_s, n_l) F(\lambda), \tag{2.15}$$

where a_{sph} is the radius of spherical particle; $Q_s(a_{sph}, n_S, n_I)$ is the scattering efficiency factor; $F(\lambda)$ is the packing factor of the particles; n_s is the refractive index of the particles; n_I is the refractive index of the ISF; φ is the volume fraction of particles for each layer. For dermal layers the scattering coefficient was calculated as [60]:

$$\mu_s(\lambda) = \frac{\varphi}{\pi\alpha_c^2} 2a_c Q_s(a_c, n_s, n_I) F(\lambda), \tag{2.16}$$

where a_c is the radius of cylindrical particles. Both the effective size of the particles and their packing factor were calculated by the minimization of the target function

$$\mathrm{TF}(a(\lambda), F(\lambda)) = (\mu_s^{\mathrm{mod}} - \mu_s^{\mathrm{Mie}})^2 + (g^{\mathrm{mod}} - g^{\mathrm{Mie}})^2, \tag{2.17}$$

where μ_s^{mod} and g^{mod} correspond to the data calculated according to Eqs. 2.12 and 2.13 for each layer; μ_s^{Mie} and g^{Mie} are the scattering coefficient (Eqs. 2.15 and 2.16) and the anisotropy factor calculated for each layer on the basis of Mie theory. To minimize the target function the Nelder and Mead simplex method described in detail in Ref. [62] has been used.

The influence of clearing agent on the skin optical properties was simply modeled by increasing of ISF index of refraction up to 1.45. It was assumed that effective size, packing factor, and index of refraction of the scatterers have not being changed at the immersion optical clearing.

For modeling of tattoo, an absorbing layer in the form of cross with thickness 50 μm and size 1 × 1 cm^2 was added to the skin model. Total area of the modeled skin sample was 3 × 3 cm^2. Absorption coefficient of the cross was equal to absorption coefficient of ink, i.e., 11770, 10776, 8673, 7872, 6150, and 5253 cm^{-1} at wavelengths 470, 532, 650, 694, 850, and 1064 nm, respectively. Scattering properties of this layer was taken as similar to the scattering properties of reticular dermis. The depth of ink location in the model was chosen as 0.5 or 1 mm.

The MC simulation has been performed on the basis of the algorithm presented in Ref. [7]. For the calculation of the photon fraction absorbed in tattoo area the following procedure was used: When a photon trajectory passed through the tattoo area, parameter A_t (the photon fraction absorbed in tattoo area) increased

on $w\mu_a/(\mu_a + \mu_s)$ at the each act of interaction [7], where w is the current weight of photon packet, and μ_a and μ_s are the coefficients of absorption and scattering in the given point, respectively. After the detection of all photon packets, the value A_t was summed over all packets and normalized to the total weigh of the packets, which were used for the simulation. A new propagation direction of the scattered photon packet was determined according to the Henyey–Greenstein scattering phase function:

$$f_{HG}(\theta) = \frac{1}{4\pi} \frac{1 - g^2}{(1 + g^2 - 2g\cos\theta)^{3/2}}, \tag{2.18}$$

where θ is the polar scattering angle. The distribution over the azimuthal scattering angle was assumed as uniform.

For the simulation of skin images with tattoo 25×10^6 photon packets was used. Photons normally incident on the skin surface were uniformly distributed over the area 3×3 cm^2. For the detection of backscattered photons, this area (3×3 cm^2) was separated on the grid with area of the grid cells of 0.01 mm^2. When backscattered photon went out, its weigh was recorded to the array cell, which corresponded to the coordinates of the point of going out, then was summed over all packets. After the finishing of the simulation it was normalized to the average weight of the incident packets upon corresponding area.

The thicknesses and refractive indices of skin layers used in the MC simulations are presented in Table 2.3. Without optical clearing for each wavelength and each skin layer, absorption coefficient, scattering coefficient, and anisotropy factor were calculated using Eqs. 2.10, 2.12, and 2.13, respectively. At the immersion skin optical clearing, scattering coefficient and anisotropy factor of each skin layer were calculated using Eqs. 2.15 and 2.16.

2.5.4 Results of MC Modeling and Discussion

Monte Carlo simulations of reflectance spectra and images of the human skin with black tattoo localized in reticular dermis at the depth of 0.5 and 1.0 mm are presented in Figs. 2.13 and 2.14 [49,50]. In Fig. 2.13, the reflection spectra are shown: for the intact skin without tattoo (curves 1); for the skin with tattoo located at the depth of 0.5 mm (a) and 1.0 mm (b) (curves 2); with skin layers over or

under tattoo are immersed (curves 3 and 4, respectively); and totally immersed skin without/with tattoo (curves 5 and 6, respectively). In all cases the subcutaneous adipose tissue layer was not immersed. The shape of the intact skin reflectance spectrum is determined by light scattering of tissue components and absorption of melanin, blood hemoglobin with bands at 416, 542, and 575 nm, and water

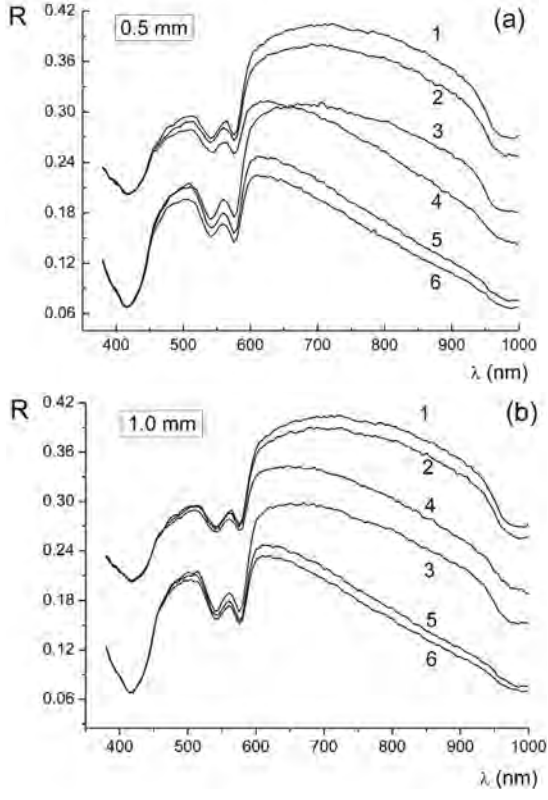

Figure 2.13 MC simulated human skin reflectance spectra with a black color tattoo at a depth of 0.5 (a) and 1.0 mm (b): (1) normal skin; (2) skin with tattoo; (3) skin layers above tattoo are immersed by an OCA (model of topical OCA administration); (4) skin layers under tattoo (between tattoo and subcutaneous adipose tissue) are immersed by an OCA (model of intradermal injection of an OCA); (5) and (6) all skin layers from the surface up to subcutaneous adipose tissue are immersed by an OCA (model of combined OCA administration—topical and via injection): (5) normal skin, (6) skin with tattoo [49].

at 980 nm. The presence of tattoo reduces the skin reflectance due to light absorption by the ink pigment. For smaller pigment location depth, the skin reflectance decreases more significantly. The modeling demonstrates well that optical clearing of different skin layers, upper and lower tattoo location, allows for control of skin reflectivity in a rather wide range within the visible and NIR wavelengths. However, to use IOC effects in practice to image and/or ablate absorbing inhomogeneity like tattoo or tumor, we are able to introduce and calculate two more parameters, such as image contrast K and fraction of light absorbed by this inhomogeneity A [49,50].

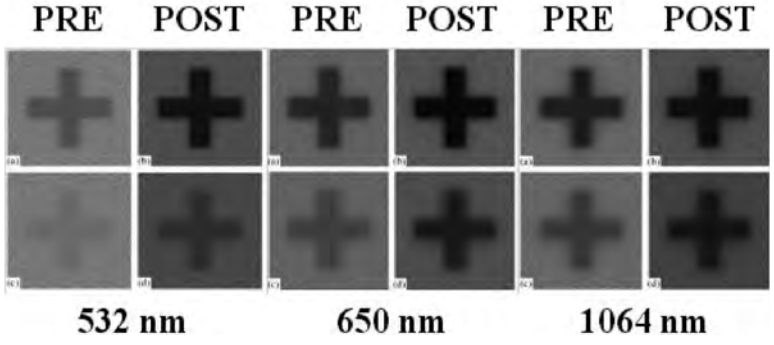

Figure 2.14 Three sets of MC simulated skin tattoo images at the wavelengths 532, 650, and 1064 nm: (a, b) the depth of the tattoo is 0.5 mm and (c, d) 1.0 mm; the size of the tattoo is 1×1 cm^2; (a, c) no clearing; (b, d) skin layers above the tattoo are optically cleared (model of topically applied immersion agent) [50].

The images, presented in Fig. 2.14, were simulated using optical properties of skin at λ = 532 nm, 650 nm, and 1064 nm. The left images of each set correspond to the skin with tattoo, as the right images correspond to the same skin but with optically cleared skin layers above the tattoo in accordance with the model of topically administered immersion agent [50]. The tattoo image boundaries without IOC look rather blurred due to high light scattering by the upper tissue layers. The simulation of photon migration in skin has shown that the immersion of the upper skin layers is more efficient for image contrast improvement and increasing of the number of photons absorbed by the tattoo.

As it follows from Fig. 2.14, the optical clearing of the upper skin layers significantly enhances the image contrast, which improves the tattoo localization and imaging. The image contrast can be estimated as:

$$K = \frac{(R_1 - R_2)}{(R_1 + R_2)}, \tag{2.19}$$

where R_1 and R_2 are the skin reflectance outside the tattoo area and inside it, respectively.

Results of tattoo image contrast calculations for normal and optically cleared skin are also presented in Table 2.4 and Fig. 2.15. It is well seen that contrast of the tattoo images increases with the wavelength of illuminating light with some saturation in the NIR spectral range. At the same time, clearing efficiency expressed as a ratio of the contrast images of tattoo in immersed skin to the contrast images of tattoo in native skin, somewhat decreases with the wavelength. However, the efficiency is still very high, especially for deeper tattoo localization, and less dependent on the wavelength in the range above 700 nm (Fig. 2.15).

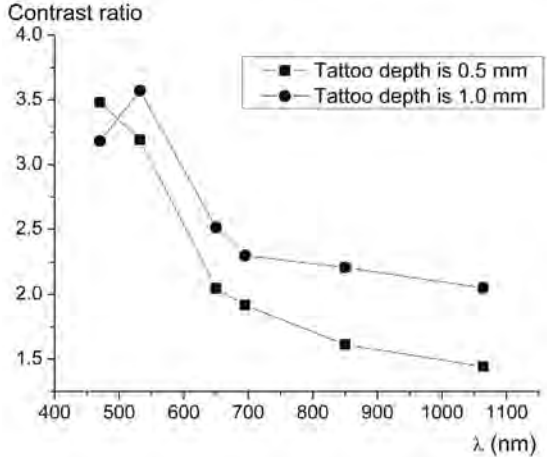

Figure 2.15 The wavelength dependences of contrast ration K_{POST}/K_{PRE} for tattoo images (POST and PRE are after and before optical clearing (model of OCA topical application), respectively) [50].

Table 2.4 Result of MC simulation of image contrast of 1 mm-depth skin tattoo pre- and post-OCA topical application [50]

Wavelength (nm)	Immersed skin, K_{POST}	Native skin, K_{PRE}	K_{POST}/K_{PRE}
470	0.070	0.022	3.182
532	0.100	0.028	3.571
650	0.284	0.113	2.513
694	0.382	0.166	2.301
850	0.380	0.172	2.209
1064	0.371	0.181	2.050

Figure 2.16 presents the spectral dependences of the fraction of photons absorbed by the skin layer with tattoo A at depths of 0.5 and 1 mm. Curves 1 and 5, which describing intact and totally immersed skin without tattoo, are very similar to each other and close to zero due to small absorption of native skin in this range and this particular localization—this is a base line for modeling of absorbed fraction by tattoo. The presence of tattoo changes

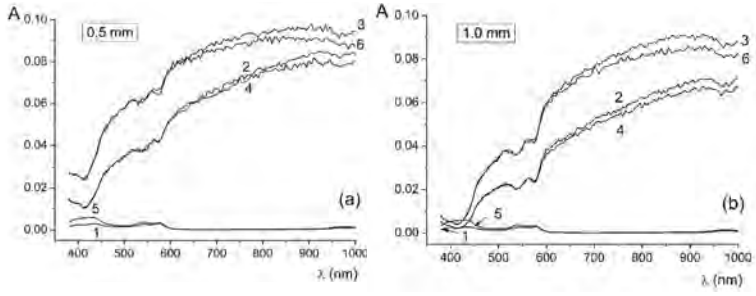

Figure 2.16 Result of MC simulation of absorbed photon fraction in the black tattoo area of skin at a depth of 0.5 (a) or 1.0 mm (b) under the different conditions: (1) normal skin; (2) skin with tattoo; (3) skin layers above tattoo are immersed by an OCA (model of topical OCA administration); (4) skin layers under tattoo (between tattoo and subcutaneous adipose tissue) are immersed by an OCA (model of intradermal injection of an OCA); (5) and (6) all skin layers from the surface up to subcutaneous adipose tissue are immersed by an OCA (model of combined OCA administration—topical and via injection): (5) normal skin, (6) skin with tattoo [49].

the spectral dependence of the fraction of absorbed photons in accordance with the absorption spectrum of the used ink or dye. The immersion of layers under tattoo reduces the number of photons absorbed in the given area, which is well seen in Fig. 2.16, curves 4. At the same time, if only upper layers over the tattoo are cleared, a significant number of photons propagate through the upper layers almost without scattering and are absorbed in the tattoo area. Photons that have passed through the absorbing layer to down skin layers, which are not cleared, can be effectively backscattered and also absorbed by the tattoo. The fraction of photons absorbed in the wavelength range from 600 to 1000 nm increases upon clearing of upper skin layers on average by 30% and 40% for tattoos at depths of 0.5 and 1 mm, respectively. Thus, for deeply located tattoo this method of clearing is more efficient.

Table 2.5 summarizes data of IOC efficiency for a 1 mm-depth location of tattoo. It is seen that the absorbed fraction increases with the increase of the wavelength similar to the image contrast behavior (see Table 2.4), and the ratio of the light fraction absorbed in tattoo embedded in immersed skin to the fraction for tattoo embedded in the native skin decreases with the wavelength (see Fig. 2.17). The ratio decreases from 1.588 (λ = 470 nm) to 1.197 (λ = 1064 nm) for tattoo located at the depth of 1.0 mm and from 1.633 (λ = 470 nm) to 1.082 (λ = 1064 nm) for tattoo located at the depth of 0.5 mm. That is related to general decrease of skin scattering for the longer wavelengths; so less overall photons circulate within absorbing layer and are absorbed by tattoo.

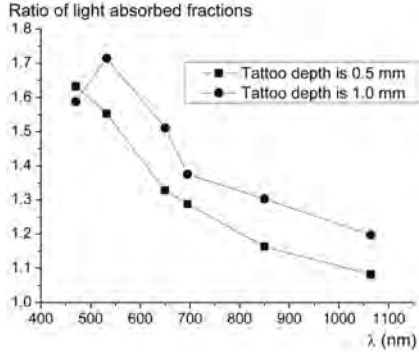

Figure 2.17 The wavelength dependences of the ratio of light absorbed fractions by tattoo A_{POST}/A_{PRE} (POST and PRE are after and before optical clearing, respectively) [50].

However, the efficiency of IOC is still good to provide laser thermolysis of tattoo or other skin absorbing abnormality for a number of wavelengths. Basing on literature data for different laser systems it was estimated [50] that to achieve the similar tattoo damage, which can be obtained without skin optical clearing, at optical clearing the density of laser energy can be reduced in dependence on the tattoo localization depth up to 50–60% for the blue-green spectral range, 30–40% for the red, and 10–20% for the NIR.

Table 2.5 MC simulation of light absorbed fraction A by tattoo located at 1.0 mm depth

Wavelength, nm	A_{PRE}	A_{POST}	A_{POST}/A_{PRE}
470	0.017	0.027	1.588
532	0.021	0.036	1.714
650	0.045	0.068	1.511
694	0.056	0.077	1.375
850	0.066	0.086	1.303
1064	0.071	0.085	1.197

Note: A_{PRE} is for normal skin; A_{POST} is for upper skin layers immersed by an OCA [50].

2.6 Summary

Facing the problem of combining properties of optical radiation and the ability to cope with the parameters of biological tissues, which are anticipated to vary spatially and temporally, as well as individually, the MC technique becomes a primary tool in biophotonics and biomedical optics. The developed O3MC tool can be used for direct on-line real-time simulation of human skin spectra and colors depending on the blood, water, melanin content. The geometry of particular probes is taken into account for skin spectra simulation as well as controllable and selective immersion optical clearing of skin layers. With the further development of the technique additional parameters such as spatial distribution of blood vessels, tissue shrinkage and swelling, red blood cells aggregation and their velocity will be included. In addition, by applying recently developed approach of handling polarization [45,46] the MC can be used for direct simulations of sampling

volume for various probe geometry, skin reflectance spectra for non-, co- and cross- polarized light, fluorescence spectra modeling, and other. We believe with the new developments the MC technique will find a number of new straightforward applications related to the non-invasive optical based skin studies.

Acknowledgments

This study was supported in part by the Ministry of Business, Innovations, and Employment of New Zealand; by the University of Oulu, Finland, project FiDiPro TEKES 40111/11; as well as by a Grant of the President of the Russian Federation no. NSh-1177.2012.2 and by state contracts of the Russian Federation nos. 14.V37.21.0728 and 14.V37.21.0563.

References

1. Tuchin VV (ed.) (2010). *Handbook of Photonics for Biomedical Science*, CRC Press, Taylor & Francis Group, London.
2. Doronin AV and Meglinski IV (2011). Online object oriented Monte Carlo computational tool for the needs of biomedical optics, *Biomed Opt Express,* **9**, 2461–2469.
3. Doronin AV and Meglinski IV (2011). Monte Carlo simulation of photon migration in turbid random media based on the object-oriented programming paradigm, in *Biomedical Applications of Light Scattering V* (Wax AP and Backman V, eds), Proc. SPIE, 7907, 790709.
4. Doronin AV and Meglinski IV (2010). GPU-accelerated Object-Oriented Monte Carlo modeling of photon migration in turbid media, in *Optical Technologies in Biophysics and Medicine* XII (Tuchin VV and Genina EA, eds), *Proc*. *SPIE*, 7999, 79990K.
5. Dolin LS (2009). Development of radiative transfer theory as applied to instrumental imaging in turbid media, *Phys-Usp,* **52**, 519–526.
6. Martelli F, Del Bianco S, Ismaelli A, and Zaccanti G (eds) (2009). *Light Propagation through Biological Tissue and Other Diffusive Media: Theory, Solutions, and Software*, SPIE Press.
7. Wang LH, Jacques SL, and Zheng LQ (1995). MCML—Monte Carlo modeling of photon transport in multilayered tissues, *Comput Meth Prog Bio,* **47**, 131–146.

8. Meglinski IV and Matcher SJ (2001). Modeling the sampling volume for the skin blood oxygenation measurements, *Med Biol Eng Comput*, **39**, 44–50.
9. Meglinski IV (2001). Modeling the reflectance spectra of the optical radiation for random inhomogeneous multi-layered highly scattering and absorbing media by the Monte Carlo technique, *Quantum Electron*, **31**, 1101–1107.
10. Meglinski IV and Matcher SJ (2003). Computer simulation of the skin reflectance spectra, *Comput Meth Prog Bio*, **70**, 179–186.
11. Churmakov DY, Meglinski IV, and Greenhalgh DA (2004). Amending of fluorescence sensor signal localization in human skin by matching of the refractive index, *J Biomed Opt*, **9**, 339–346.
12. Churmakov DY, Meglinski IV, Greenhalgh DA, and Piletsky SA (2003). Analysis of skin tissues spatial fluorescence distribution by the Monte Carlo simulation, *J Phys D: Appl Phys*, **36**, 1722–1728.
13. Meglinski IV and Churmakov DY (2004). Spatial localization of biosensor fluorescence signals in human skin under the effect of equalization of the refractive Index of the surrounding medium, *Opt Spectrosc*, **96**, 946–951.
14. Meglinski IV, Kirillin M, Kuzmin VL, and Myllyla R (2008). Simulation of polarization-sensitive optical coherence tomography images by a Monte Carlo method, *Opt Lett*, **33**, 1581–1583.
15. Kirillin M, Meglinski I, Sergeeva E, Kuzmin VL, and Myllyla R (2010). Simulation of optical coherence tomography images by Monte Carlo modeling based on polarization vector approach, *Opt Express*, **18**, 21714–21724.
16. Kirillin MY, Priezzhev AV, and Meglinski IV (2006). Effect of photons of different scattering orders on the formation of a signal in optical low-coherence tomography of highly scattering media, *Quantum Electron*, **36**, 247–252.
17. Romanov VP, Churmakov DY, Berrocal E, and Meglinski IV (2004). Low-order light scattering in multiple scattering disperse media, *Opt Spectrosc*, **97**, 796–802.
18. Meglinski IV, Romanov VP, Churmakov DY, Berrocal E, Jermy MC, and Greenhalgh DA (2004). Low and high orders light scattering in particulate media, *Laser Phys Lett*, **1**, 387–390.
19. Kuzmin VL and Meglinski IV (2004). Coherent multiple scattering effects and Monte Carlo method, *JETP Lett*, **79**, 109–112.

20. Meglinski IV, Kuzmin VL, Churmakov DY, and Greenhalgh DA (2005). Monte Carlo simulation of coherent effects in multiple scattering, *Proc Roy Soc A*, **461**, 43–53.
21. Kuzmin VL and Meglinski IV (2010). Anomalous polarization phenomena of light scattered in random media, *J Exp Theor Phys*, **137**, 742–753.
22. Kuzmin VL and Meglinski IV (eds) (2010). *Helicity Flip of Backscattered Circularly Polarized Light*, *Proc. SPIE*, 7573, 75730Z.
23. Kuzmin VL and Meglinski IV (2007). Coherent effects of multiple scattering for scalar and electromagnetic fields: Monte-Carlo simulation and Milne-like solutions, *Opt Commun*, **273**, 307–310.
24. Kuzmin VL, Meglinski IV, and Churmakov DY (2005). Stochastic modeling of coherent phenomena in strongly inhomogeneous media, *J Exp Theor Phys*, **101**, 22–32.
25. Berrocal E, Meglinski IV, Greenhalgh DA, and Linne MA (2006). Image transfer through the complex scattering turbid media, *Laser Phys Lett*, **3**, 464–468.
26. Berrocal E, Sedarsky D, Paciaroni M, Meglinski IV, and Linne MA (2007). Imaging through the turbid scattering media: part I: experimental and simulated results for the spatial intensity distribution, *Opt Express*, **15**, 10649–10665.
27. Boas DA, Culver JP, Stott JJ, and Dunn AK (2002). Three dimensional Monte Carlo code for photon migration through complex heterogeneous media including the adult human head, *Opt Express*, **10**, 159–170.
28. Ramella-Roman J, Prahl S, and Jacques S (2005). Three Monte Carlo programs of polarized light transport into scattering media: part I, *Opt Express*, **13**, 4420–4438.
29. Fang Q (2010). Mesh-based Monte Carlo method using fast ray-tracing in Plücker coordinates, *Biomed Opt Express*, **1**, 165–175.
30. Shen H and Wang G (2011). A study on tetrahedron-based inhomogeneous Monte Carlo optical simulation, *Biomed Opt Express*, **2**, 44–57.
31. Meglinski IV, Kirillin M, and Kuzmin VL (2008). The concept of a unified modelling of optical radiation propagation in complex turbid media, *Proc. SPIE*, 7142, 714204.
32. Schach S (ed) (2006). *Object-Oriented and Classical Software Engineering*, Seventh Ed., McGraw-Hill, New York.
33. McConnell S (ed) (2004). *Code Complete*, 2nd ed., Microsoft Press, Redmond.

34. Kirk DB, Hwu WW (eds) (2010). *Programming Massively Parallel Processors: A Hands-on Approach*, Morgan Kaufmann Publishers, Burlington.

35. Sanders J and Kandrot E (ed) (2010). *CUDA by Example: An Introduction to General-Purpose GPU Programming*, Addison-Wesley, Boston.

36. CUDA Programming Guide 4.0; CUBLAS Library; CUFFT Library; CURAND Library (2011). NVIDIA Corporation.

37. Shklar L and Rosen R (eds) (2009). *Web Application Architecture: Principles, Protocols and Practices*, John Wiley & Sons Ltd, Chichester.

38. Doronin AV (2011). GPU-Accelerated Biophotonics & Biomedical Optics, NVIDIA Corporation, interview, Aug. 28.

39. Doronin A and Meglinski I (2012). Peer-to-Peer Monte Carlo simulation of photon migration in topical applications of biomedical optics, *J Biomed Opt*, **17**, 090504.

40. Churmakov DY, Meglinski I, and Greenhalgh DA (2002). Influence of refractive index matching on the photon diffuse reflectance, *Phys Med Biol*, **47**, 4271–4285.

41. Jacques S (2013). Optical properties of biological tissues: a review, *Phys Med Biol*, **58**, R37–R61.

42. Saidi I, Jacques S, and Tittel F (1995). Mie and Rayleigh modeling of visible-light scattering in neonatal skin, *Appl Opt*, **34**, 7410–7418.

43. Donner G and Jensen HW (2006). A spectral BSSRDF for shading human skin, in: *Rendering Techniques 2006: 17th Eurographics Workshop on Rendering*, pp 409–418.

44. Petrov GI, Doronin A, Whelan HT, Meglinski I, and Yakovlev VV (2012). Human tissue colour as viewed in high dynamic range optical spectral transmission measurements, *Biomed Opt Express*, **3**, 2154–2161.

45. Churmakov DY, Kuzmin VL, and Meglinski IV (2006). Application of the vector Monte Carlo method in polarization optical coherence tomography, *Quantum Electron*, **36**, 1009–1015.

46. Kuzmin VL and Meglinski IV (2009). Backscattering of linearly and circularly polarized light in randomly inhomogeneous media, *Opt Spectrosc*, **106**, 257–267.

47. McNichols RJ, Fox MA, Gowda A, Tuya S, Bell B, and Motamedi M (2005). Temporary dermal scatter reduction: quantitative assessment and implications for improved laser tattoo removal, *Lasers Surg Med*, **36**, 289–296.

48. Fox AM, Diven, DG, Sra K, Boretsky A, Poonawalla T, Readinger A, Motamedi M, and McNichols RJ (2009). Dermal scatter reduction in human skin: a method using controlled application of glycerol, *Lasers Surg Med*, **41**, 251–255.

49. Genina EA, Bashkatov AN, Tuchin VV, Altshuler GB, and Yaroslavski IV (2008). Possibility of increasing the efficiency of laser-induced tattoo removal by optical skin clearing, *Quant Electron*, **38**(6), 580–587.

50. Bashkatov AN, Genina EA, Tuchin VV, and Altshuler GB (2009). Skin optical clearing for improvement of laser tattoo removal, *Laser Phys*, **19**(6), 1312–1322.

51. Tuchin VV (ed) (2006). *Optical Clearing of Tissues and Blood*, PM154, SPIE Press, Bellingham.

52. Genina EA, Bashkatov AN, and Tuchin VV (2010). Tissue optical immersion clearing, *Expert Rev Med Devices*, **7**(6), 825–842.

53. Larin KV, Ghosn MG, Bashkatov AN, Genina EA, Trunina NA, and Tuchin VV (2012). Optical clearing for OCT image enhancement and in-depth monitoring of molecular diffusion, *IEEE J Select Tops Quant Electron*, **18**(3), 1244–1259.

54. Zhu D, Larin KV, Luo Q, and Tuchin VV (2013). Recent progress in tissue optical clearing, *Laser Photonics Rev*, 1–26.

55. Tuchin VV, Altshuler GB, Gavrilova AA, Pravdin AB, Tabatadze D, Childs J, and Yaroslavsky IV (2006). Optical clearing of skin using flashlamp-induced enhancement of epidermal permeability, *Lasers Surg Med*, **38**(9), 824–836.

56. Genina EA, Bashkatov AN, Korobko AA, Zubkova EA, Tuchin VV, Yaroslavsky I, and Altshuler GB (2008). Optical clearing of human skin: comparative study of permeability and dehydration of intact and photothermally perforated skin, *J Biomed Opt*, **13**(2), 021102-1–8.

57. Genina EA, Bashkatov AN, Dolotov LE, Maslyakova GN, Kochubey VI, Yaroslavsky IV, Altshuler GB, and Tuchin VV (2013). Transcutaneous delivery of micro- and nanoparticles with laser microporation, *J Biomed Opt*, **18**(11), 111406-1–9.

58. Altshuler G, Smirnov M, and Yaroslavsky I (2005). Lattice of optical islets: a novel treatment modality in photomedicine, *J Phys D: Appl Phys*, **38**, 2732–2747.

59. Bashkatov AN, Zhestkov DM, Genina EA, and Tuchin VV (2005). Immersion optical clearing of human blood in the visible and near infrared spectral range, *Opt Spectrosc*, **98**(4), 638–646.

60. Bohren CF and Huffman DR (eds) (1983). *Absorption and Scattering of Light by Small Particles*, Wiley, New York.
61. Tuchin VV (ed) (2007). *Tissue Optics: Light Scattering Methods and Instruments for Medical Diagnosis*, PM 166, SPIE Press, Bellingham.
62. Bunday B (ed) (1984). *Basis Optimization Methods*, Edward Arnold, London.